PAPER

Check for updates

Unveiling the potential of a self-activated BCNO afterglow phosphor for superior visibility in extremely low-light environments†

K. A. K. Durga Prasad, Aachal A. Sharma, Payal P. Pradhan, M. Rakshita and D. Haranath [ID] *

The development of versatile luminescent materials with afterglow properties is one of the ways to meet the increasing demands for energy saving. Attempts were being made to develop even self-activated afterglow phosphors by introducing defects in the host lattice, but the number of such phosphors known is limited. Herein, a self-activated rare-earth-free blue-emitting boron carbon oxynitride (BCNO) afterglow phosphor is developed by the sol–gel auto-combustion method at low temperatures (∼700 °C). The formation of BCNO phosphor and its crystal structure are confirmed by XRD and supported by FTIR and XPS analysis. The developed BCNO phosphor features rod-like morphology with high-intensity luminescence properties. Optical and luminescence studies provide insight into the visible light-induced afterglow property of this phosphor. Time-resolved photoluminescence studies showcase that the phosphor has an afterglow duration of around 30 minutes with optimal intensity. Thermoluminescence studies revealed the trap depth of the defects responsible for the afterglow properties and provided an insight into the afterglow mechanism of the phosphor. The BCNO phosphor, when applied over the white-based paint on a vitrified tile, can easily be seen in extremely dark conditions. The visible light-induced afterglow property of the BCNO phosphor has rendered it a prominent material in low-light environments.

1. Introduction

Energy saving has become one of the major global challenges affecting humanity in the last two decades.[1,2] Consequently, a great deal of research is being done all around the world to develop new functional materials and effective energy sources.[3,4] Afterglow phosphors or persistent phosphors belong to one such class of energy-saving materials that consistently arouse the researchers in the area of material science, physics, chemistry, and even biology due to their intriguing optical behaviour and their widespread use.[5,6] Afterglow phosphors are of particular interest because of their ability to retain and release light energy for periods of time ranging from a few seconds to several hours, even after the source of stimulating radiation has been switched off.[7,8] From the past few decades of development, afterglow phosphors have been employed from the initial civil use, *i.e.*, decoration, emergency signages, safety displays, alternating current white LEDs, *etc.*, to a broad range of well-developed scientific application domains, including

environmental engineering, biomedicine, clinical medicine, and life sciences.[6,7,9–11]

Even though the phenomenon of afterglow has been known to mankind for centuries, the bolognian stone was the first material known to exhibit afterglow in the literature.[6] By the end of the nineteenth century, copper-activated zinc sulphide (ZnS : Cu) was the most promising afterglow phosphor, which was employed in some practical applications.[12] But the preparation of ZnS : Cu phosphor is so laborious as it involves toxic sulfide gases such as H_2S or CS_2 because of the ability of ZnS to be converted into zinc oxide at high temperatures. On the other hand, the highly sensitive nature of this ZnS : Cu phosphor with the surrounding moisture made it chemically unstable. The above facts of ZnS : Cu limit its potential for commercial growth.[6]

However, the development of rare earth-activated strontium aluminate afterglow phosphor ($SrAl_2O_4 : Eu^{2+}$, Dy^{3+}) by Matsuzawa *et al.* in 1996 has outperformed the existing ZnS : Cu afterglow phosphor and brought significant progress in terms of lifetime as well as intensity.[13] The development of $SrAl_2O_4 : Eu^{2+}$, Dy^{3+} substantially enhanced the scientific interest in developing afterglow phosphors that could replace ZnS : Cu. Since 1996, many afterglow phosphors have been developed with oxide, aluminate, and silicate-based host lattices activated with one or more rare earth ions.[14] This scenario created a huge demand for the existing rare earth ions, which made the

Luminescent Materials and Devices (LMD) Group, Energy Materials and Devices Laboratory, Department of Physics, National Institute of Technology Warangal, Hanumakonda 506004, Telangana, India. E-mail: haranath@nitw.ac.in; Tel: +91 995 810 1115

preparation of afterglow phosphors so expensive. Additional problems pertaining to rare earth ions include their scarcity in the world market, expensive production, and safety hazards from their mining. While research on replacing rare-earth-activated phosphors is still in its early stages, people all over the world have begun to look into the possibility. Materials in this class, known as rare-earth-free phosphors, are gaining a lot of attention. So, there is a need to develop rare-earth-free afterglow phosphors that are highly stable and less expensive. However, researchers across the world started their contribution towards the development of rare earth free afterglow phosphors.

Many rare-earth-free afterglow phosphor materials, such as CdS, CdSe, and ZnS : Mn, *etc.*, have been developed and commercialized, each having a different emission in the visible region. But these phosphors are composed of substances that are hazardous to the environment over an extended period of time, such as selenium (Se), sulfur (S), and cadmium (Cd). Because of this, the quest for more affordable phosphors devoid of toxic elements has been a significant problem in the research and development of efficient afterglow phosphors. Boron carbon oxynitride (BCNO) is one such rare earth-free material derived from the addition of carbon and oxygen atoms into the boron nitride.[15] It can be self-activated to produce radiative transitions between the energy levels created by the defects formed during the synthesis of the material. It is environmentally friendly as it can be produced at lower temperatures (less than 1000 °C) under ambient atmospheric conditions. BCNO is a typical wide band gap semiconductor whose band gap value ranges from 3.22 eV to 5.9 eV, enabling it to produce tunable photoluminescence from blue to red wavelength regions.[16] In addition to photoluminescence, BCNO phosphor is known to exhibit afterglow in the green region, whose wavelength is centred at 520 nm for 2 hours.[5] But to date, the reports of BCNO afterglow phosphor exhibiting colors other than green are limited, and most of them are excited in the UV region but not by visible light.

In this work, we synthesized a strong fluorescent, self-activated, blue-emitting BCNO afterglow phosphor by the sol–gel route, followed by auto combustion at low temperatures (~700 °C). The raw materials used for the synthesis of this phosphor are cost-effective, and the developed phosphor can emit afterglow property for ~30 minutes after the source of excitation is ceased. The afterglow property of the developed phosphor can be induced by both UV and visible light, which is a crucial aspect of this phosphor that is not present in the existing phosphors, and allows it to be employed in civil areas. The following sections provide a comprehensive description of the synthesis process along with the various characterization techniques employed. Furthermore, the synthesized phosphors, in association with white paint, are coated on a tile that can be used in low-light environments.

2. Experimental section

2.1. Starting materials

Analytical grade boric acid (H_3BO_3) (EMPLURA, 99.5%), poly ethylene glycol (PEG) (SRL), and urea or carbamide

(NH_2CONH_2) (FINAR, 99%) are used as the starting materials, which can act as a source of boron, carbon, and nitrogen, respectively. The essential oxygen for the formation of the required compound can be derived from all three sources, as they are oxygen-rich. The synthetic process involved no further purification of starting materials.

2.2. General synthesis strategy

The inexpensive nature and instant availability of the starting materials themselves indicate the cost-effectiveness of the material; we still made it more facile by adopting the sol–gel route, followed by the auto-combustion method to synthesize our phosphor. The schematic procedure followed for the synthesis of the BCNO specimens is displayed in Fig. 1. A series of BCNO specimens have been synthesized by mixing the initial raw materials in an agate mortar pestle for five minutes to get a homogeneous solid solution of precursors. Thoroughly ground raw materials are dissolved in water and stirred continuously at 80 °C until the solution becomes gel. The gel is then placed on a preheated auto combustion chamber, which then undergoes exothermic reactions to get phosphor powder. The obtained powder is then placed in a porcelain crucible and transferred into a microcontroller-based programmable muffle furnace. The specimens were synthesized by heating the above mixture to 700 °C for half an hour in an ambient atmosphere. Initially, the PEG concentration of the specimens is optimized by fixing the mole ratio of B/N. This is because the PEG, being a carbon source, results in the formation of black carbon products. Excess PEG concentration leads to carbonization of the specimen, which imparts a black body color that will diminish the photoluminescence (PL) of the specimen. After optimizing the PEG concentration, we studied the PL by altering the mole percentage of nitrogen source (2.5, 5, 7.5, 10, 12.5, 15, 20, 25) and labelled them as U-1 to 8, respectively. The yield of the synthesized specimens is observed to be much lower than the whole sum of initial raw materials because of the evolution of ammonia (NH_3) and carbon dioxide (CO_2) at elevated temperatures (~700 °C).

2.3. Characterization techniques

Several material characterization techniques have been adopted for a comprehensive study of the different properties of the above-synthesized phosphor specimens. The crystal structure, composition, and phase purity of the BCNO specimens were determined with the aid of an X-ray diffractometer (Panalytical, X-pert powder) using Bragg Brentano geometry. Fourier transform infrared (FTIR) spectroscopy analysis was performed for the synthesized specimen using an FTIR alpha spectrometer (Bruker, Alpha II) instrument. The chemical state of the as-obtained specimen was analyzed with X-ray photoelectron spectroscopy (XPS) analysis. The as-obtained specimen was characterized by a field emission scanning electron microscope (FESEM) to conduct morphological and microstructural analysis. Optical studies were done by recording UV-visible spectra with a high-resolution UV-Vis-NIR spectrophotometer (Agilent Technologies, Carry 5000). The photoluminescence (PL)
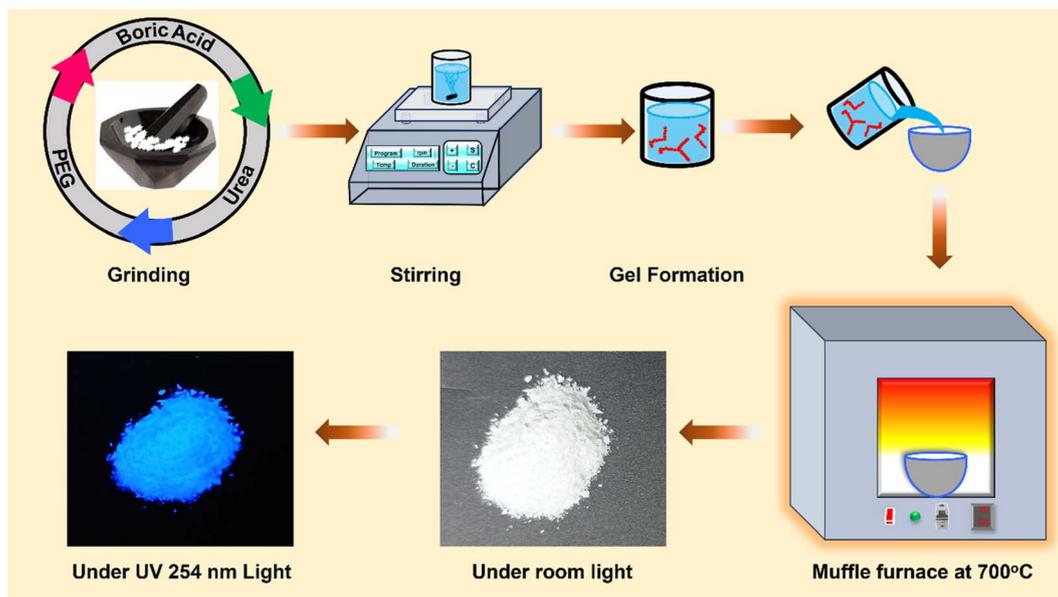
Fig. 1 Schematic representation of the synthesis procedure of BCNO afterglow phosphor.

properties, encompassing excitation, emission, and lifetime spectra, were meticulously recorded using a high-sensitivity fluorescence spectrophotometer (Hitachi, F-4700). The thermoluminescence (TL) glow curve was measured with a dedicated TL research reader (Nucleonix Systems, TL1009I). All these characterizations were conducted at room temperature (~25 °C). Among the various specimens synthesized in this study, only the U-8 sample exhibited the desired afterglow property. Given that the manuscript focuses on the self-activated afterglow property of BCNO phosphor, we have specifically investigated the structural, optical, PL, and TL properties of all samples and highlighted the U-8 sample in detail.

3. Results and discussion

3.1. Structural investigation

It is essential to have the basic information regarding the arrangement of atoms in a crystalline material, as it greatly influences its physical and chemical properties, which determine the real-time application of the material. As the uniqueness of the array of atoms in crystalline materials leads to distinctive X-ray diffraction (XRD) patterns having unique values of interplanar separation and relative intensities, it provides a fingerprint to identify the material. So, the preliminary characteristics of the material, like crystal structure, phase composition, and average crystallite size of the as-obtained BCNO specimen, were identified with the aid of the powder X-ray diffraction (PXRD) technique. Fig. 2 displays the PXRD plot of the synthesized BCNO specimen recorded within the scan range 10 to 60° by using Cu Kα_1 source having wavelength $\lambda = 1.54$ Å. It is evident from the PXRD pattern, which indicates the presence of both B_2O_3 as well as BN phases in the synthesized BCNO specimen, and is similar to the earlier

observations.[17] The broad peaks at the 2θ positions 26.9°, 43.1° and 54.3° are induced by the formation of turbostratic boron nitride (t-BN) in the BCNO specimen. The above characteristic peaks of the t-BN are indexed as (002) plane an unresolved (10) plane, which comprises of (100) and (101) planes of h-BN and (442) plane, respectively, according to the Joint Committee on Powder Diffraction Standards (JCPDS) reference No. 073-2095.[18] Apart from t-BN, the two more sharp and intense diffraction peaks exist at 2θ position 14.56°, 27.93°, 30.59° and 40.01° are indexed as (111), (310), (222) and (420) crystal planes respectively (JCPDS No. 06-0297) which signifies the existence of boric oxide (B_2O_3) in cubic phase in the final product.[17] The formation of B_2O_3 may be a consequence of the thermal decomposition of unreacted boric acid. The presence of both t-BN and cubic B_2O_3 in the specimen from the above XRD results ensures the successful formation of the required BCNO specimen *via* a solid-state reaction. The exothermic reaction that has
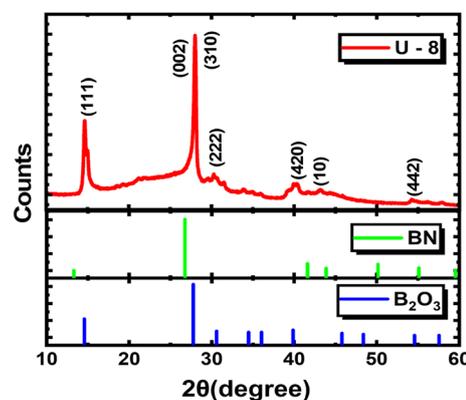

Fig. 2 XRD pattern of the BCNO afterglow phosphor with corresponding JCPDS cards of BN and B_2O_3.

occurred between urea and B_2O_3 might be the source of the formation of t-BN in the BCNO specimens. It is evident from the XRD that the B_2O_3 phase dominates the t-BN phase in the BCNO specimen due to the difference in the melting points of urea (133 °C) and H_3BO_3 (171 °C). The low melting point of urea makes it volatile under ambient atmosphere and doesn't provide enough nitrogen for the formation of the t-BN phase during the reaction. The average crystallite size of the U-8 phosphor specimen is determined to be 11.03 nm by using the Debye–Scherrer equation given by

$$D = \frac{k\lambda}{B \cos\theta}$$

where D is the average crystallite size of the phosphor, λ is the wavelength of the X-rays used, k is the Scherrer constant, B is the full width at half maximum of the peaks, and θ is the Bragg's angle.

The existence of different functional groups or the structural information and the composition of a material can be known by characterizing it with the FTIR spectroscopy technique, as it provides a better understanding of the bonding present between the atoms of the material. In the current study, FTIR analysis was performed on the synthesized phosphor specimen in the mid-infrared region (400–4000 cm^{-1}), and the corresponding spectra are shown in Fig. 3. It is obvious that different characteristic absorption bands have been observed in the spectra and are comprehensively validated to understand the evolution of the BCN phase from the B_2O_3 phase. The band assignment of different absorption peaks of the synthesized BCNO specimen (U-8) is summarized in Table 1. For this compound, strong bands are observed corresponding to B–N, B–O, and B–N–B bonds. The band observed at 1454 cm^{-1} corresponds to the B–N out-of-plane stretching vibration mode and confirms the existence of a sp^2 hybridized B–N bond.[19–21] The absorption band positioned at 783 cm^{-1} is assigned to the B–N–B in-plane bending vibration mode and sp^2 hybridized B–N linkage.[22–24] The presence of B–N stretching and B–N–B bending modes in the specimen supports the formation of the BN phase. The absorption of B–N broadens, indicating that C has been introduced into BN.[25] The absorption peak centered at 1030 cm^{-1} is assigned to the B–O–B bond.[26] Two absorption peaks positioned at 547 cm^{-1} and 647 cm^{-1} correspond to the

Table 1 Band assignment of the FTIR spectrum of U-8 phosphor

Peaks (cm^{-1})	Band assignment
1454 cm^{-1}	B–N out-of-plane stretching vibration
783 cm^{-1}	B–N–B in plane bending vibration
1030 cm^{-1}	B–O–B bond
547 cm^{-1}, 647 cm^{-1}	Vibration mode of the B–O bond
882 cm^{-1}	Stretching vibrations of the B–O bond
1195 cm^{-1}	B–C stretching vibration
3221 cm^{-1}	Stretching vibrations of the O–H group

vibration mode of B–O bonds.[27,28] The presence of a sharp peak at 882 cm^{-1} is attributed to the stretching vibrations of the B–O bond, which indicates the existence of residual tetrahedral BO_4 units and supports the formation of the B_2O_3 phase as discussed in the XRD analysis.[29] The formation of residual tetrahedral BO_4 units may be a consequence of the decomposition of boric acid into boric anhydride, which, upon heat treatment, cleaves some of the B–O–B bonds into B–O$^-$ bonds and finally coordinates together to form BO_4.[30] One sharper band was also detected at 1195 cm^{-1} for the B–C stretching vibrational mode.[25,31] The peaks at 2258 cm^{-1} and 2359 cm^{-1} are induced by the C≡N and C=O stretching vibrations, respectively.[19] The absorption peak at 3221 cm^{-1} indicates that the stretching vibrations of the O–H group in the phosphor synthesized at elevated temperatures are due to the adsorption of moisture from the surroundings of the environment.[28] Owing to the above FTIR analysis, it is observed that both the C and O elements are bound to the B and N in the structure of the synthesized phosphor specimen.

Further, XPS analysis has been carried out on the phosphor specimen in order to get a detailed overview of the specimen structure, its elemental composition, and the bonding between them. It is an efficient tool to analyse the surface by incident X-rays on the sample and detect the number of electrons emitted at a certain binding energy, which confirms the presence and chemical state of a particular element. Fig. 4(a) displays the survey scanned XPS spectra of the as-obtained phosphor specimen which indicates the presence of all the elements that made up the required phosphor specimen and shows strong peaks centered at 194.08 eV, 285.08 eV, 399.08 eV and 532.42 eV which are corresponding to the characteristic binding energies of the B, C, N and O 1s region respectively. The individual XPS profiles of the B 1s, C 1s, N 1s, and O 1s are deconvoluted with the aid of Gaussian fitting as shown in Fig. 4(b–e) to get the information regarding the bonding characteristics of the constituent elements as well as the structure of the phosphor by fine-scanned XPS spectra. The deconvoluted fine-scanned B 1s profile given in Fig. 4(b) shows three peaks centered at 190.71, 193.51, and 194.49 eV, which are assigned to the B–C–N bond, BO_x, and B–O of the B_2O_3 phase, respectively.[32–35] The characteristic peak centered at 284.64 eV in the deconvoluted fine-scanned C 1s profile given in Fig. 4(c) is attributed to the C–C bond, which is in good agreement with the observed binding energy of graphene (284.9 eV).[35] The other two peaks at 285.97 and 288.80 eV are ascribed to sp^2 hybridized C–N or C≡N bond
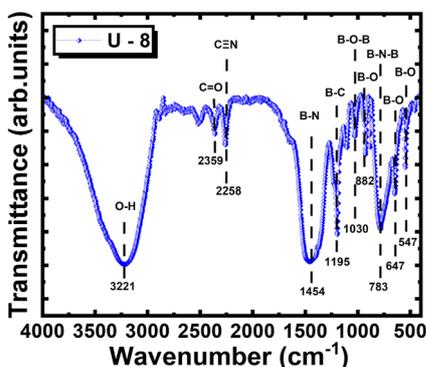

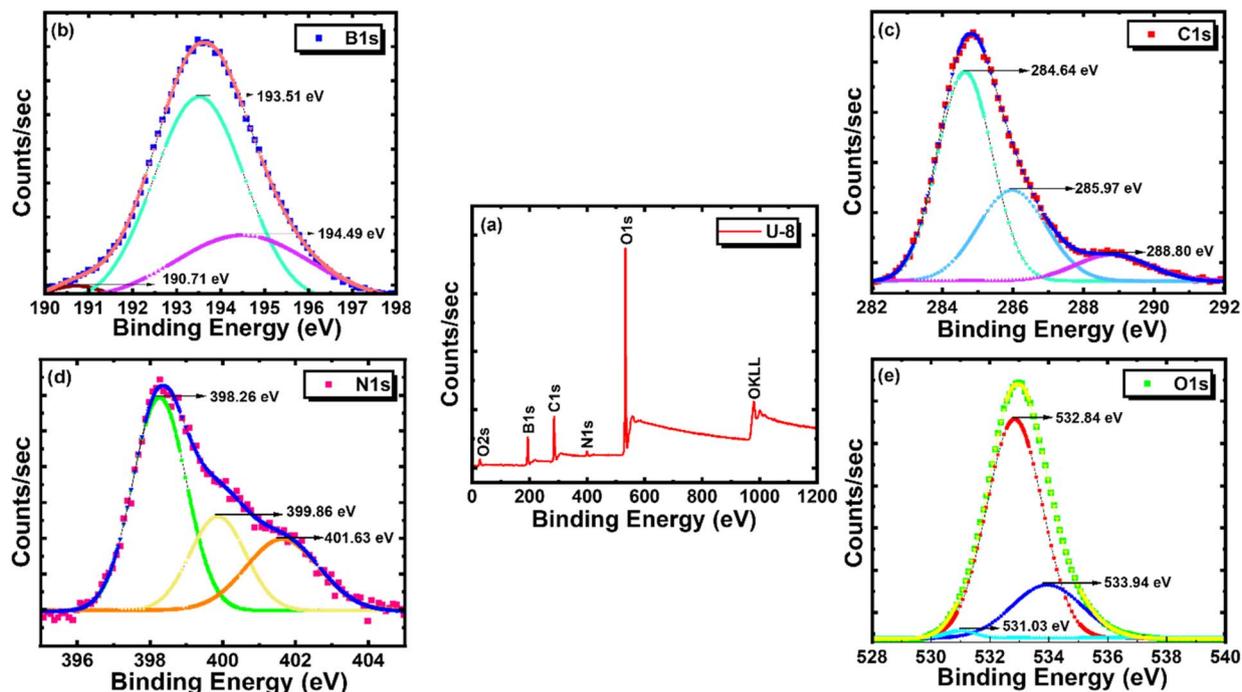**Fig. 3** FTIR spectra of the BCNO phosphor.

Fig. 4 (a) XPS survey spectrum of BCNO phosphor. High-resolution individual spectra of (b) B 1s, (c) C 1s, (d) N 1s, and (e) O 1s.

and C–O bond of oxygenated carbon, respectively.[36] The peaks associated with the binding energies 398.26, 399.86, and 401.63 eV in the deconvoluted fine-scanned N 1s profile given in Fig. 4(d) correspond to the pyridinic N, C–B–N, and graphitic N bonds, respectively.[37,38] Furthermore, the characteristic binding energy peak of the O 1s profile is deconvoluted, as shown in Fig. 4(e), and consists of three typical peaks centered at 531.03, 532.84, and 533.94 eV, which are assigned to the O–C, O–B, and C=O, respectively.[35] Perhaps the above analysis validates the existence of each of the components (B, C, N, O) and different stable bindings between them that made the phosphor.

3.2. Particle characterization

Generally, the luminescent characteristics of a phosphor are mostly dependent on its surface morphology as well as the particle size distribution. Fig. 5(a and b) shows the FESEM images of the U-8 phosphor specimen. From Fig. 5(a), it is visible that the particles of the as-synthesized phosphor exhibit uniform flower-like surface morphology at a higher scale (100 μm) and lower magnification (1k×). When the scale bar is reduced (40 μm) and magnification is increased (4k×), as shown in Fig. 5(b), it is observed that each flower is composed of several rod-like structures having a wide variation in their length and diameter. The petals (rods) of the flower are connected through their wider bases, and the diameter of each petal varies from the tips to the bases. The average diameter of these petals at their tips is estimated to be around 1.66 μm. The anisotropic growth of the prolonged rod-like structures may provide a large surface-to-volume ratio, which can enhance the absorption of light and then improve the intensity of the emitted light of the synthesized phosphors. However, rod-like

morphology exhibits fewer surface defects, which improves effective radiative transitions and provides necessary traps to acquire efficient afterglow. Fig. 5(c) displays the energy dispersive X-ray (EDS) spectrum of the BCNO phosphor, which results when characteristic X-rays that carry the information about the elemental composition of the sample are emitted on interacting with high-energy electrons. By identifying the wavelength of the emitted X-rays, the composition of the phosphor will be quantified.[39] From EDS analysis, the mass percentages of the elements boron, carbon, nitrogen, and oxygen are found to be 20.52%, 7.91%, 14.86%, and 56.71%, respectively, in the as-obtained BCNO phosphor. The absence of any additional elements confirmed that BCNO phosphor had formed. The percentage of oxygen content is the highest compared to other elements. The percentage composition of the BCNO phosphor obtained from EDS measurement is compared with its actual molar mass percentage composition and is given in Table 2. The percentage of molar mass composition is given by the ratio of the molar mass of each element to the total molar mass of all the elements present in the compound. Fig. 5(d) depicts the comprehensive elemental mapping of all the elements conducted on a specific area of the BCNO specimen. The mapping of individual elements displayed in Fig. 5(e–h) indicates the uniform distribution of every species in the specimen.

3.3. Optical analysis

UV-Vis-NIR spectroscopy, usually referred to as absorption spectroscopy, has been performed on the BCNO specimen under diffuse reflectance (DRS) mode to characterize its optical properties and to determine its band gap. Fig. 6(a) shows the absorption spectrum of the BCNO specimen in the wavelength
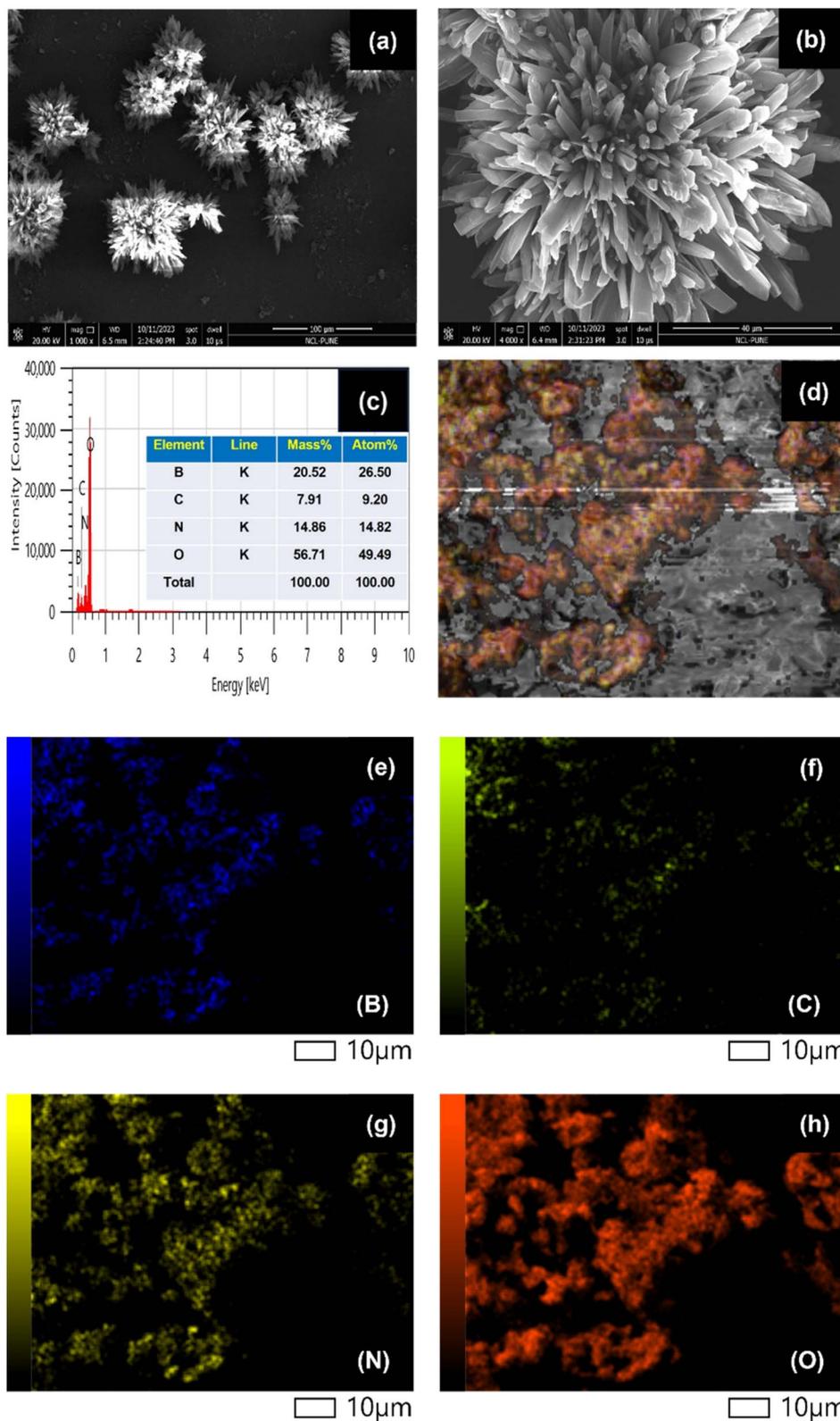
Fig. 5 (a and b) FESEM images taken at different magnifications, (c) EDAX spectrum, and (d–h) elemental mapping images of the BCNO phosphor.

range of 220–800 nm. The phosphor shows a pronounced absorption band in the UV region, with an extended tail that suggests notable absorption into the visible range as well. The

broad absorption band in the UV region (220–350 nm) centered at 288 nm corresponds to the formation of intrinsic defects, *i.e.*, paramagnetic centers like nitrogen vacancies in the BCNO

Table 2 Comparison of elemental composition percentage measured from EDS and actual molar mass

Element	EDS measured elemental composition (wt%)	Actual molar mass composition (wt%)
B	20.52	20.5
C	7.91	22.7
N	14.86	26.5
O	56.71	30.3

phosphor. The extended tail in the visible region ($\sim$400 nm) is attributed to the electron transition between the defect states arising from the incorporation of carbon and oxygen in the BCNO specimen.[19,24,40–42] The absorption curve becomes flat beyond 500 nm wavelength, indicating high reflectivity of the specimen. The body color of the phosphor specimen takes on a faint green hue in the daylight due to its ability to absorb wavelengths up to 450 nm in the visible region. The optical band gap energy of the BCNO phosphor specimen is estimated using Tauc plots and the Kubelka–Munk formula as follows:

$$(\alpha h \nu)^2 = k(h\nu - E_g)$$

where α, h, ν, and k indicate the molar extinction coefficient, Planck's constant, frequency, and constant independent of energy, respectively. Fig. 6(b) depicts the plot of the transformed Kubelka–Munk function $(\alpha h \nu)^2$ *versus* light energy $(h\nu)$. The extrapolation of the straight-line portion in the Tauc plot to the light energy axis using linear fitting yields an inflection point on this curve whose abscissa is directly associated with the optical band gap (E_g) value, *i.e.*, 3.66 eV for the as-obtained BCNO phosphor. According to the previous reports, the calculated optical band gap value for pure boron nitride (BN) in its bulk form is between 5–6 eV.[16,43–46] The deviation of the band gap value of BCNO phosphor from BN is due to the incorporation of impurities such as C and O, which will create defect energy levels below the bottom of the conduction band, which shifts the absorption to the longer wavelength side and thereby decreases the band gap. The band gap of the as-obtained phosphor is dependent on the concentration of carbon and oxygen impurities and the position of their energy levels below

the conduction band. The existence of these impurities enables the phosphor to have a broad range of absorption, extending it into the visible region. The detailed study of optical properties could be done in conjunction with PL spectra.

3.4. Photoluminescent characteristics

The origin of different electronic excitations and the corresponding radiative emissions from a specimen can be understood by conducting PL spectroscopy. The excitation and emission studies of the BCNO phosphors are systematically investigated by varying the molar percentage of nitrogen source in the initial raw materials while maintaining the carbon/boron (C/B) molar ratio at 7.5×10^{-4}. The photoluminescence excitation (PLE) spectra of the as-obtained BCNO phosphors are recorded at an emission wavelength of 392 nm. As seen from Fig. 7(a), the PLE spectra of all the phosphors are very broad, spanning multiple wavelengths from UV ($\sim$225 nm) to the visible region ($\sim$400 nm). It is obvious from plot Fig. 7(a) that the shape of the PLE spectra is similar for all the specimens, which implies that the origin of excitation centers is identical for all, irrespective of their ratio of initial raw materials. There exist two excitation peaks, one broad peak centered around 285 nm, and a shoulder peak was observed around 366 nm. The high-intensity broad peak at 285 nm is attributed to the transition of charge carriers to intrinsic defects, *i.e.*, nitrogen vacancies formed during the synthesis of phosphors. Whereas, the shoulder at 366 nm corresponds to the excitation of electrons from carbon and oxygen-related impurity levels to the higher energy levels.[24,40] The PLE intensity of the specimens increased as we went from U_1 to U_7, and then decreased for U_8. The intensity drop in the U_8 specimen may be due to the decrease in the concentration of nitrogen vacancies.[24] The above PLE data are in good agreement with the information deduced from the optical analysis. The ability of the as-obtained BCNO phosphor to have absorption and excitation wavelengths in the visible region, as demonstrated from optical and excitation spectra, made it a potential candidate for low-light environments.

Fig. 7(b) displays the PL emission spectra of all the BCNO specimens derived from various concentrations of nitrogen source under an excitation wavelength of 285 nm. There exists
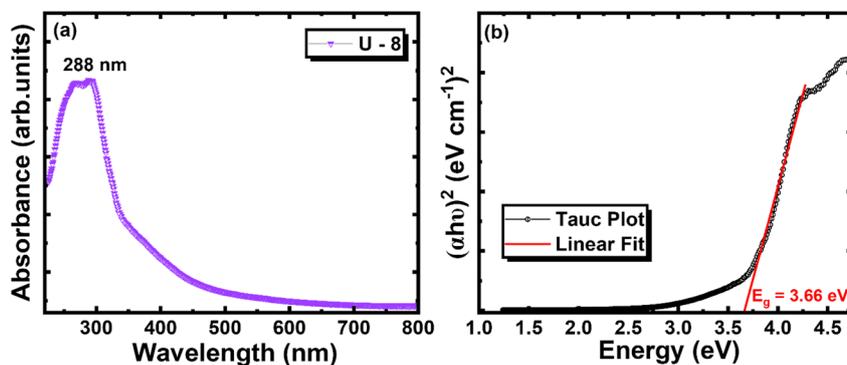

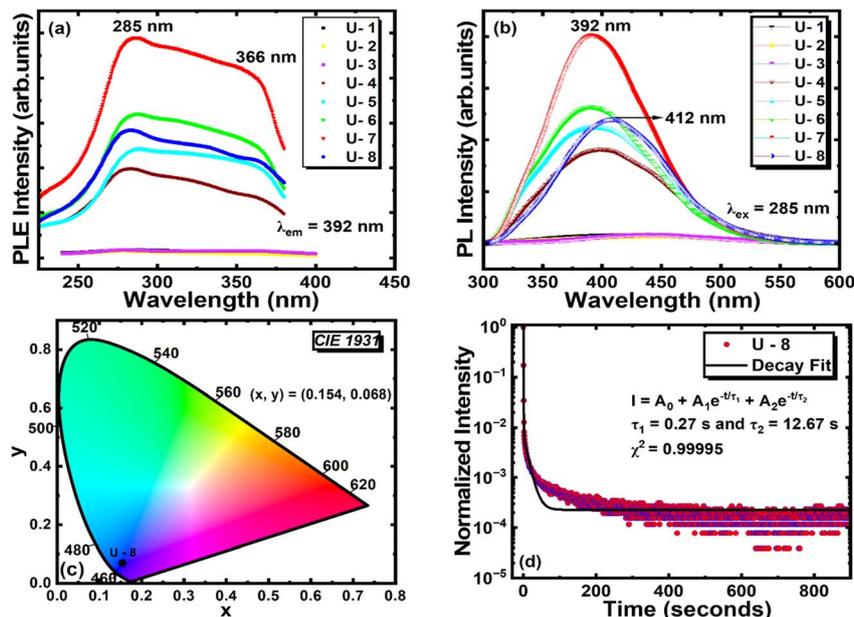**Fig. 6** (a) UV-Vis DRS spectra and (b) Tauc plot of the BCNO phosphor.

Fig. 7 (a) PLE spectra, (b) PL spectra, (c) CIE chromaticity diagram, and (d) TRPL spectra of the BCNO phosphor.

a broad peak in the wavelength range 300–550 nm for all the specimens. The values of peak emission wavelength and external quantum yield (EQY) of all the phosphor specimens are given in Table 3. The red shift observed in U-2 and U-3 samples with the increase in urea concentration may be due to the broadening of nitrogen and carbon defect levels between the valence and conduction bands, which reduces the band gap. Conversely, the subsequent blue shift with higher urea concentration may stem from the nitridation of the samples, which induces structural distortion and increases the band gap.[47] The PL intensity of the specimens increases as the nitrogen concentration in the initial raw materials increases and reaches a maximum for U[7]. A sudden drop in PL intensity is observed for the U[8] specimen if a further increment in nitrogen concentration beyond U[7] has been made. This scenario may be attributed to the reduced number of radiative relaxations of the charge carriers due to a decrease in the concentration of nitrogen vacancies. In addition to a decrease in the PL intensity, the wavelength of the U[8] specimen shifted from 392 to 412 nm

when compared to the remaining specimens. The slight red shift of emission spectra in the U[8] specimen may be a result of varied concentrations of carbon and oxygen-related impurities.[48] Despite the low heat conductivity of BCNO phosphor, the heat flow in these phosphors is limited to the surface of the specimen, which leads to uneven heating.[49] Due to this, the bonds formed in the specimen are weak, and the probability of having impurities and the formation of defects in the BCNO is higher. The presence of these carbon and oxygen-related impurities creates some energy levels below the conduction band, and the position of these levels is dependent on the concentration of the impurities.[18,40] So, the increase in the amount of these carbon and oxygen impurities or defects shifts the emission spectra to a longer wavelength.[24] This interpretation is consistent with studies done by Watanabe *et al.* and Ogi *et al.* that show the carbon and/or nitrogen concentration of the particles in the BCN atomic structure affects the shift in luminescence color of BCN materials.[50–52] The EQY of the U-8 afterglow sample has been compared to the existing blue-emitting phosphors and is given in Table 4.

The color coordinates of the as-obtained U[8] specimen are derived by plotting the PL data of the phosphor excited at 285 nm by using the CIE 1931 (Commission Internationale de L'Eclairage) chromaticity diagram, as shown in Fig. 7(c). By its peak emission at 412 nm, the phosphor's CIE color coordinates ($x = 0.154$, $y = 0.068$) fall in the blue region of the visible spectrum. Chromaticity makes it possible to quantify the quality of color irrespective of the intensity of the material. Substituting the color coordinates (x, y) in the following formula can determine the color quality of the BCNO specimen.

Table 3 Peak emission wavelength and EQY values of the BCNO phosphor specimens

Sample name	Peak emission wavelength (nm)	External quantum yield (%)
U-1	415	0.71
U-2	448	0.55
U-3	442	0.22
U-4	392	6.61
U-5	392	6.66
U-6	392	1.92
U-7	392	20.32
U-8	412	10.28

$$\text{Color purity (\%)} = \frac{\sqrt{(x_s - x_e)^2 + (y_s - y_e)^2}}{\sqrt{(x_d - x_e)^2 + (y_d - y_e)^2}} \times 100$$

Table 4 Quantum yield comparison of BCNO phosphor (current work) with existing literature

S. no	Phosphor	λ_{em} (nm)	Quantum yield (%)	Reference
01	BCNO	469	79	52
02	BCNO	460	9.3	53
03	BCNO	440	23	54
04	BCNO	450	60	55
05	BCNO	460	52.2	56
06	BCNO	452	99	24
07	$BaMgAl_{10}O_{17}:Eu^{2+}$	450	95	52
08	$ZnS:Ag$	450	75	6
09	BCNO	412	10.28	This work

where $(x_e, y_e) = (0.33, 0.33)$ are coordinates of the ideal white light, $(x_s, y_s) = (0.154, 0.068)$ are the as-obtained phosphor color coordinates, and $(x_d, y_d) = (0.134, 0.041)$ are the dominant wavelength coordinates. The color purity of the phosphor is found to be 90.43%.

A light source's color appearance at a particular temperature, measured in degrees Kelvin (K), is described by Correlated Color Temperature (CCT). The CCT value of the as-obtained phosphor can be calculated according to the following analytical equation given by McCamy, and it is found to be 1703.07 K.[57,58]

$$CCT = -449n^3 + 3525n^2 - 6823n + 5520.33$$

To study the afterglow properties of a phosphor, it is essential to understand the recombination kinetics of the photo-generated charge carriers. This can be done by conducting time-resolved photoluminescence (TRPL) spectroscopy measurements on the synthesized phosphor. The lifetimes of different photon-assisted relaxations of the charge carriers can be known from the TRPL measurements, which are beneficial in determining the efficiency of afterglow phosphors. In the current work, the U_8 phosphor specimen is observed to emit afterglow property, and the rest of the phosphors don't have detectable afterglow emission. So, the afterglow decay curve of the U_8 phosphor is recorded at the peak wavelength of 412 nm after continuous excitation of the specimen with a monochromatic light at 365 nm for 5 minutes. As shown in Fig. 7(d), with the immediate removal of the excitation source, the afterglow intensity of the phosphor drops rapidly due to the continuous release of electrons from the energy levels created by traps due to thermal activation from the surrounding environment. Followed by rapid decay, the phosphor undergoes a steady decay process with an optimal intensity whose afterglow remains discernible with minimal intensity (0.32 mcd m^{-2}) around 30 minutes to the dark-adapted human eye. The lifetime data of the afterglow decay process of U_8 phosphor can be obtained by fitting the decay curves with the available exponential decay functions. The decay curve of the U_8 phosphor is well fitted to the bi-exponential function, whose analytical equation is given as follows:

$$I(t) = I_0 + A_1 e^{-\frac{t}{\tau_1}} + A_2 e^{-\frac{t}{\tau_2}}$$

where I is the afterglow intensity of the phosphor given as a function of time t, and I_0 is at time $t = 0$. The constants A_1 and A_2 are the weighing parameters measured at time $t = 0$; the exponential components τ_1 and τ_2 represent lifetimes of the different decay processes, which can be extracted from the above curve fitting equation. The lifetime of phosphor is generally described as the amount of time it takes to drop its peak PL intensity value to $1/e$ of its initial value following the cessation of the excitation source. The lifetime values ($\tau_1 = 0.27$ s and $\tau_2 = 12.66$ s) obtained from the decay equation suggest that the afterglow behaviour of the phosphor consists of an initial rapid decay process followed by a slow decay process. The slow and fast decay processes correlated to the lifetime values $\tau_1 = 0.27$ s and $\tau_2 = 12.66$ s can be due to the shallow and deep traps, respectively, created by the defects formed during the formation of BCNO phosphor. Intrinsic defects such as nitrogen vacancies, substitutional defects such as carbon-substituted boron or nitrogen, and B/O related defects acting as trapping and detrapping sites would create energy levels in the band gap of the BCNO phosphor, which in turn affect the afterglow lifetimes of the phosphor. The presence of the B_2O_3 phase can also alter the band structure of the BCNO phosphor, which can create potential traps controlling the charge carrier dynamics and affect the afterglow performance of the phosphor. Despite the discussed defects, the intrinsic and extrinsic characteristics, quality, and composition of the material greatly alter the value of the decay components. The time-resolved photoluminescence spectra for all synthesized samples, and the corresponding lifetime data, have been included as Fig. S1–S8 in the ESI.†

3.5. Thermoluminescence studies

Usually, the charge traps created in the host lattice during the synthesis of phosphor are responsible for the occurrence of its afterglow phenomenon. These charge traps may be the defects formed in the phosphor during synthesis or the dopants that are intentionally added to the host lattice. Different properties, such as nature, depth, and concentration of charge traps, will affect the lifetime characteristics of a phosphor[59–61] The traps in the phosphor are filled with the charge carriers while exposing it to the external radiation at room temperature. The filled traps release the charge carriers on the subsequent rise of temperature of the system above room temperature with consequent photon emission, which leads to the afterglow of phosphor. A shallow trap releases the charge carriers immediately after irradiation, leading to a rapid decay in afterglow. Whereas the deep traps accompany the slow release of charge carriers at room temperature and require more energy to escape from the traps, leading to a slow decay in afterglow.

However, for efficient afterglow emission at room temperature, the charge trap should be neither too shallow nor too deep.[62] To study the nature of the charge traps (either shallow traps or deep traps), TL characterization has been performed on the as-obtained U_8 phosphor. TL provides a better insight into

studying the underlying mechanism of afterglow phosphors by investigating the spatial distribution of energy levels created by the charge traps.

The TL glow curve of U_8 phosphor is plotted as shown in Fig. 8. Before the TL measurement, the phosphor was exposed to UV light (365 nm) for 10 minutes at room temperature, and then the temperature was raised to 300 °C at a constant rate of 3 °C s^{-1}. The information regarding the nature of the charge traps is given by the TL glow curve, in which the plot of emitted light intensity as a function of temperature (T) is drawn. A broad and high-intensity TL glow curve was observed in the temperature range of 320 to 500 K. As the temperature increases, a steady rise in the TL intensity is observed, which indicates the de-trapping of charge carriers from different traps. The probability of the de-trapping process becomes maximum at 374.15 K and decreases further beyond this temperature. The observed afterglow of the phosphor is caused by the release of the charge carriers from the traps, and the following formula may be used to approximate the depth of the traps.[63]

$$E = \frac{T_m}{500}$$

where E is the depth of the charge trap and T_m is the temperature corresponding to the maximum intensity of the TL glow curve. According to the above expression, charge traps of depth around 0.75 eV were found in the U_8 phosphor. As discussed above, the charge trap should not be too shallow or too deep for efficient afterglow performance, and the accepted optimal value of trap depths at room temperature typically ranges between 0.65 and 0.8 eV.[64] The above determined trap depth value of U_8 phosphor is in the proximity of the optimal range. This ensures an efficient trapping and de-trapping process in U_8 phosphor and therefore, exhibits considerable afterglow.

3.6. Afterglow mechanism

Since the development of afterglow phosphors, researchers have proposed many mechanisms to explain this phenomenon by adapting different hypotheses, like electron trapping, hole trapping, *etc.* But the afterglow mechanism of BCNO afterglow phosphor is still debatable due to its complex electronic structure and defect-activated luminescence. Most of the studies showcased that there exists a strong correlation between the presence of nitrogen vacancies (paramagnetic centres) and
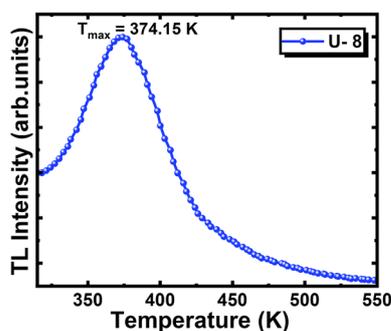
carbon impurities, which creates luminescence centres with an energy level around 4.1 eV.[45,65,66] On the other hand, a pair of carbon atoms is isoelectronic with the boron nitride (BN) molecule, thereby facilitating its incorporation into the BN lattice more easily than oxygen atoms. However, from XRD results, it is known that the majority of oxygen atoms are found with boron as boron trioxide, which acts as an interfacial zone connecting boric acid and turbostratic BN.[67] Based on these things, BCNO can be assumed as a carbon-doped boron oxy nitride compound, and the following afterglow mechanism is proposed.

Depending on the optical and photoluminescent characteristics of the BCNO phosphor specimen, an energy level diagram shown in Fig. 9 was proposed to provide an insight into the afterglow mechanism of BCNO phosphor. Following the excitation by UV light (365 nm), electron and hole pairs are generated in the BCNO phosphor. The photogenerated electrons get excited to the conduction band, resulting in the formation of holes in the valence band. Some of the excited electrons get trapped by the nitrogen vacancies, which are assumed to be shallow traps. After the cessation of the excitation source, the trapped electrons in the nitrogen vacancies are thermally activated by the surroundings and slowly released to feed the energy level created by carbon impurity, from which radiative transition takes place and consequently leads to the afterglow phenomenon of BCNO phosphor.

3.7. Potential application

Even though several studies address different aspects like synthesis, color tunability, PL performance, afterglow behavior, *etc.*, of BCNO afterglow phosphor, very few studies report their real-time potential applications, and it has not yet materialized to a greater extent. Generally, afterglow phosphors are employed in dark vision, emergency signage, safety markings, glow-in-the-dark toys, *etc.* Since afterglow phosphors are known to be used in several areas, in this work, we developed an afterglow tile that can find significant application in low-light environments. Firstly, a 4 cm × 4 cm tile is taken and thoroughly cleaned with water. Later, a fine layer of white paint is
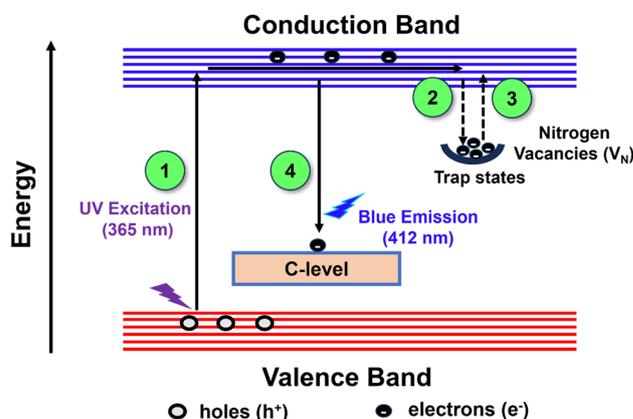

Fig. 8 TL glow curve of BCNO phosphor.
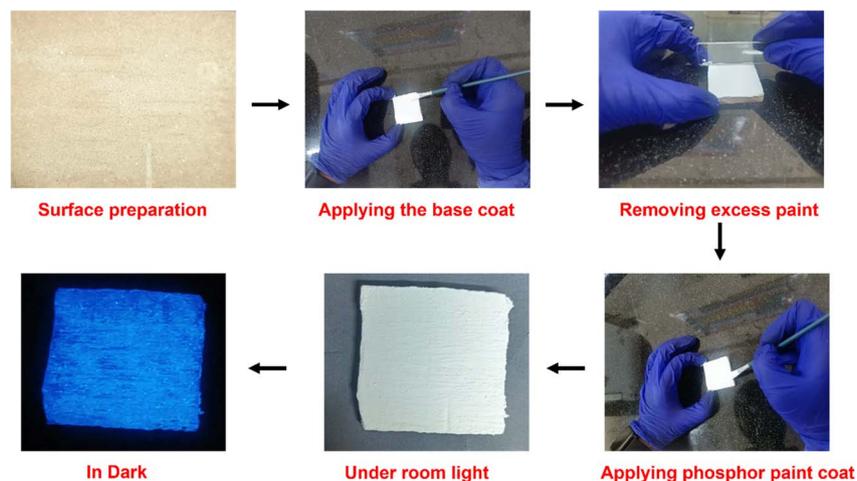

Fig. 9 Afterglow mechanism of BCNO phosphor.

Fig. 10 Sequence of steps followed to coat afterglow phosphor paint on a tile.

applied to the tile and allowed it dry. The above step is repeated three times, and the excess paint is removed by using a glass slide in order to ensure a uniform layer of white background. In the last step, the synthesized phosphor specimen mixed with the white paint is coated on the tile to acquire the afterglow property. The images of the afterglow phosphor-coated tile under daylight and in dark conditions are shown in Fig. 10. The afterglow tile, after absorbing sunlight during the day, can emit afterglow property for around half an hour in low-light environments. This afterglow tile can be used in buildings and can find potential application in low-light environments.

4. Conclusions

Self-activated, rare-earth-free, blue-emitting afterglow phosphors were prepared by the sol–gel auto combustion method at low temperatures ($\sim$700 °C) by keeping the C/B molar ratio fixed and varying the nitrogen concentration. XRD, FTIR, and XPS studies confirmed the formation as well as the crystal structure of the phosphor. FESEM images of the phosphor reveal the rod-like structures connected to form flower-like morphology, and can be correlated with the strong fluorescent nature of the phosphor. The band gap of the phosphor was found to be 3.66 eV by conducting UV-visible studies. Optical and PLE spectra show almost similar maximum absorption (288 nm) and excitation (285 nm) wavelengths, and extend their spectra into the visible region. This made the phosphor available with a visible light-induced afterglow property, which is an aspect to use it in low-light environments in civil areas. PL spectra show a broad emission centered at 412 nm, corresponding to the blue colour. TRPL studies revealed that the decay curve of the phosphor is well-fitted with the bi-exponential decay function and shows an optimal intensity around 30 minutes. TL studies indicate that the trap depth of the defects formed during the synthesis of phosphor is 0.75 eV, which lies in the optimum trap depth range (0.65–0.8 eV). A mechanism was proposed by considering electron trapping at the defect sites created by the nitrogen vacancies in order to explain the afterglow phenomenon of the BCNO phosphor. Synthesized phosphor finds potential application as an afterglow tile in low-light environments.

Data availability

The data that support the findings of this study are available from the corresponding author upon reasonable request.

Author contributions

K. A. K. Durga Prasad: data curation, methodology, investigation, formal analysis, writing paper, and editing. Aachal A. Sharma: data curation, formal analysis. Payal P. Pradhan: data curation, formal analysis. M. Rakshita: data curation, formal analysis. D. Haranath: conceptualization, funding acquisition, methodology, supervision, writing – review & and editing.

Conflicts of interest

The authors have no conflicts of interest to declare.

Acknowledgements

References

1 Q. Hassan, P. Viktor, T. J. Al-Musawi, B. Mahmood Ali, S. Algburi, H. M. Alzoubi, A. Khudhair Al-Jiboory, A. Zuhair Sameen, H. M. Salman and M. Jaszczur, The renewable energy role in the global energy Transformations, *Renew. Energy Focus*, 2024, **48**, 100545, DOI: **10.1016/J.REF.2024.100545**.

2 P. A. Owusu and S. Asumadu-Sarkodie, A review of renewable energy sources, sustainability issues and climate change mitigation, *Cogent Eng*, 2016, **3**, 1167990, DOI: **10.1080/23311916.2016.1167990**.

3 C. Z. Li, L. Zhang, X. Liang, B. Xiao, V. W. Y. Tam, X. Lai and Z. Chen, Advances in the research of building energy saving, *Energy Build*, 2022, **254**, 111556, DOI: **10.1016/J.ENBUILD.2021.111556**.

4 L. Gorina, E. Korneeva, O. Kovaleva and W. Strielkowski, Energy-saving technologies and energy efficiency in the post-COVID era, *Sustainable Dev.*, 2024, **32**, 5294–5310, DOI: **10.1002/SD.2978**.

5 X. Liu, Y. Qiao, G. Dong, S. Ye, B. Zhu, Y. Zhuang and J. Qiu, BCNO-Based Long-Persistent Phosphor, *J. Electrochem. Soc.*, 2009, **156**, P81, DOI: **10.1149/1.3082399**.

6 Phosphor Handbook, *Phosphor Handbook*, 2018. DOI: **10.1201/9781315222066**.

7 L. Wang, Z. Shang, M. Shi, P. Cao, B. Yang and J. Zou, Preparing and testing the reliability of long-afterglow SrAl2O4:Eu2+, Dy3+ phosphor flexible films for temperature sensing, *RSC Adv.*, 2020, **10**, 11418–11425, DOI: **10.1039/d0ra00628a**.

8 E. Finley, A. Mansouri Tehrani and J. Brgoch, Intrinsic Defects Drive Persistent Luminescence in Monoclinic SrAl2O4:Eu2+, *J. Phys. Chem. C*, 2018, **122**, 16309–16314, DOI: **10.1021/ACS.JPCC.8B04378**.

9 K. Van den Eeckhout, P. F. Smet and D. Poelman, Persistent Luminescence in Eu2+-Doped Compounds: A Review, *Materials*, 2010, **3**, 2536, DOI: **10.3390/MA3042536**.

10 Y. Zhu, Q. Yu, L. Zheng, Y. Yang, H. Jiang, D. Xu, N. Manh Son, L. Thi Thao Vien, L. Van Khoa Bao and N. Ngoc Trac, Synthesis of SrAl2O4: Eu2+ Dy3+ phosphorescence nanosized powder by combustion method and its optical properties, *J. Phys. Conf. Ser.*, 2009, **187**, 012017, DOI: **10.1088/1742-6596/187/1/012017**.

11 T. Peng, L. Huajun, H. Yang and C. Yan, Synthesis of SrAl2O4:Eu, Dy phosphor nanometer powders by sol–gel processes and its optical properties, *Mater. Chem. Phys.*, 2004, **85**, 68–72, DOI: **10.1016/J.MATCHEMPHYS.2003.12.001**.

12 W. Hoogenstraaten and H. A. Klasens, Some Properties of Zinc Sulfide Activated with Copper and Cobalt, *J. Electrochem. Soc.*, 1953, **100**, 366, DOI: **10.1149/1.2781134**.

13 T. Matsuzawa, Y. Aoki, N. Takeuchi and Y. Murayama, A New Long Phosphorescent Phosphor with High Brightness, SrAl2O4 : Eu2 + , Dy3 +, *J. Electrochem. Soc.*, 1996, **143**, 2670–2673, DOI: **10.1149/1.1837067**.

14 Y. Li, M. Gecevicius and J. Qiu, Long persistent phosphors - From fundamentals to applications, *Chem. Soc. Rev.*, 2016, **45**, 2090–2136, DOI: **10.1039/c5cs00582e**.

15 Q. Xue, H. Zhang, M. Zhu, Z. Wang, Z. Pei, Y. Huang, X. Song, H. Zeng and C. Zhi, Hydrothermal synthesis of blue-fluorescent monolayer BN and BCNO quantum dots for bio-imaging probes, *RSC Adv.*, 2016, **6**, 79090–79094, DOI: **10.1039/c6ra16744f**.

16 K. Watanabe, T. Taniguchi and H. Kanda, Direct-bandgap properties and evidence for ultraviolet lasing of hexagonal boron nitride single crystal, *Nat. Mater.*, 2004, **36 3**, 404–409, DOI: **10.1038/nmat1134**.

17 B. W. Nuryadin, F. A. Permatasari, A. Y. Nuryantini, I. D. Faryuni, M. Abdullah and F. Iskandar, A red emitting of manganese-doped boron carbon oxynitride (BCNO) phosphor materials: facile approach and photoluminescence properties, *RSC Adv.*, 2017, **7**, 4161–4166, DOI: **10.1039/C6RA27018B**.

18 X. Zhang, X. Jia, H. Liu, Z. Lu, X. Ma, F. Meng, J. Zhao and C. Tang, Spectral properties and luminescence mechanism of red emitting BCNO phosphors, *RSC Adv.*, 2015, **5**, 40864–40871, DOI: **10.1039/C5RA07054F**.

19 A. B. Suryamas, M. M. Munir, T. Ogi, Khairurrijal and K. Okuyama, Intense green and yellow emissions from electrospun BCNO phosphor nanofibers, *J. Mater. Chem.*, 2011, **21**, 12629–12631, DOI: **10.1039/C1JM12654G**.

20 S. Yan, X. Zhang, Z. Lu, M. Yu, X. Xu, J. Lin, Y. Fan, X. Zhang, F. Meng and C. Tang, Facile synthesis and photoluminescent properties of BCNO phosphors for white light emitting diodes application, *Ceram. Int.*, 2014, **40**, 7617–7620, DOI: **10.1016/J.CERAMINT.2013.12.020**.

21 P. B. Mirkarimi, K. F. McCarty and D. L. Medlin, Review of advances in cubic boron nitride film synthesis, *Mater. Sci. Eng., R*, 1997, **21**, 47–100, DOI: **10.1016/S0927-796X(97)00009-0**.

22 C. Tang, Y. Bando, C. Zhi and D. Golberg, Boron–oxygen luminescence centres in boron–nitrogen systems, *Chem. Commun.*, 2007, 4599–4601, DOI: **10.1039/B711807D**.

23 C. Zhi, Y. Bando, C. Tang, D. Golberg, R. Xie and T. Sekigushi, Phonon characteristics and cathodolumininescence of boron nitride nanotubes, *Appl. Phys. Lett.*, 2005, **86**, 1–3, DOI: **10.1063/1.1938002/931430**.

24 X. Zhang, Z. Lu, H. Liu, J. Lin, X. Xu, F. Meng, J. Zhao and C. Tang, Blue emitting BCNO phosphors with high quantum yields, *J. Mater. Chem. C*, 2015, **3**, 3311–3317, DOI: **10.1039/C5TC00179J**.

25 M. A. Mannan, M. Nagano, K. Shigezumi, T. Kida, N. Hirao and Y. Baba, Characterization of boron carbonitride (BCN) thin films deposited by radiofrequency and microwave plasma enhanced chemical vapor deposition, *Am. J. Appl. Sci.*, 2008, **5**, 736–741, DOI: **10.3844/ajassp.2008.736.741**.

26 M. Rong, X. Yang, L. Huang, S. Chi, Y. Zhou, Y. Shen, B. Chen, X. Deng and Z. Q. Liu, Hydrogen Peroxide-Assisted Ultrasonic Synthesis of BCNO QDs for Anthrax Biomarker Detection, *ACS Appl. Mater. Interfaces*, 2019, **11**, 2336–2343, DOI: **10.1021/ACSAMI.8B21786**.

27 L. Museur, E. Feldbach and A. Kanaev, Defect-related photoluminescence of hexagonal boron nitride, *Phys. Rev. B:Condens. Matter Mater. Phys.*, 2008, **78**, 155204, DOI: **10.1103/PHYSREVB.78.155204**.

28 M. Ren, W. Han, Y. Bai, C. Ge, L. He and X. Zhang, Melamine sponge-assisted synthesis of porous BCNO phosphor with yellow-green luminescence for Cr6+ detection, *Mater. Chem. Phys.*, 2020, **244**, 122673, DOI: **10.1016/J.MATCHEMPHYS.2020.122673**.

29 D. Singh, K. Singh, G. Singh, Manupriya, S. Mohan, M. Arora and G. Sharma, Optical and structural properties of ZnO-

PbO-B2O3 and ZnO-PbO-B2O3-SiO2 glasses, *J. Phys.:Condens. Matter*, 2008, **20**, 075228, DOI: **10.1088/0953-8984/20/7/075228**.

30 D. Haranath, P. Sharma, H. Chander, A. Ali, N. Bhalla and S. K. Halder, Role of boric acid in synthesis and tailoring the properties of calcium aluminate phosphor, *Mater. Chem. Phys.*, 2007, **101**, 163–169, DOI: **10.1016/J.MATCHEMPHYS.2006.03.003**.

31 C. Ren, X. Zhang, L. Zhou, Z. Lu, J. Lin, X. Xu, L. Li, X. Zhang, Y. Xue, F. Meng, J. Zhao and C. Tang, Preparation optimization and spectral properties of BCNO phosphors with high quantum efficiency, *J. Lumin.*, 2014, **153**, 338–342, DOI: **10.1016/J.JLUMIN.2014.03.044**.

32 W. J. Pan, J. Sun, H. Ling, N. Xu, Z. F. Ying and J. D. Wu, Preparation of thin films of carbon-based compounds, *Appl. Surf. Sci.*, 2003, **218**, 298–305, DOI: **10.1016/S0169-4332(03)00622-6**.

33 M. Nizam Uddin, I. Shimoyama, Y. Baba, T. Sekiguchi, M. Nagano and J. Appl Phys, X-ray photoelectron spectroscopic observation on B–C–N hybrids synthesized by ion beam deposition of borazine, *J. Vac. Sci. Technol., A*, 2005, **23**, 497–502, DOI: **10.1116/1.1894667**.

34 L. Bois, P. L'Haridon, Y. Laurent, X. Gouin, P. Grange, J. F. Létard, M. Birot, J. P. Pillot and J. Dunoguès, Characterization of a boro-silicon oxynitride prepared by thermal nitridation of a polyborosiloxane, *J. Alloys Compd.*, 1996, **232**, 244–253, DOI: **10.1016/0925-8388(95)01982-0**.

35 S. Sekar, P. Gawas, S. V. Bhat and V. Nutalapati, Highly fluorescent 2D-BCNO sheets based chemical sensor for selective detection of the explosive Dunnite and 4-nitrophenol in aqueous medium, *Environ. Sci.:Nano*, 2021, **8**, 2908–2919, DOI: **10.1039/D1EN00391G**.

36 Y. Kang, Z. Chu, D. Zhang, G. Li, Z. Jiang, H. Cheng and X. Li, Incorporate boron and nitrogen into graphene to make BCN hybrid nanosheets with enhanced microwave absorbing properties, *Carbon N. Y.*, 2013, **61**, 200–208, DOI: **10.1016/J.CARBON.2013.04.085**.

37 J. O. Hwang, J. S. Park, D. S. Choi, J. Y. Kim, S. H. Lee, K. E. Lee, Y. H. Kim, M. H. Song, S. Yoo and S. O. Kim, Workfunction-tunable, N-doped reduced graphene transparent electrodes for high-performance polymer light-emitting diodes, *ACS Nano*, 2012, **6**, 159–167, DOI: **10.1021/NN203176U**.

38 J. Heber, Nobel Prize 2014: Akasaki, Amano & Nakamura, *Nat. Phys.*, 2014, **10**, 791, DOI: **10.1038/nphys3147**.

39 S. Nasrazadani and S. Hassani, Modern analytical techniques in failure analysis of aerospace, chemical, and oil and gas industries, *Handb. Mater. Fail. Anal. with Case Stud. from Oil Gas Ind.*, 2016, 39–54, DOI: **10.1016/B978-0-08-100117-2.00010-8**.

40 X. Zhang, L. Li, Z. Lu, J. Lin, X. Xu, Y. Ma, X. Yang, F. Meng, J. Zhao and C. Tang, Effects of Carbon and Oxygen Impurities on Luminescence Properties of BCNO Phosphor, *J. Am. Ceram. Soc.*, 2014, **97**, 246–250, DOI: **10.1111/JACE.12645**.

41 X. Liu, S. Ye, Y. Qiao, G. Dong, Q. Zhang and J. Qiu, Facile synthetic strategy for efficient and multi-color fluorescent BCNO nanocrystals, *Chem. Commun.*, 2009, **0**, 4073–4075, DOI: **10.1039/B904567H**.

42 J. Tzadikov, M. Auinat, J. Barrio, M. Volokh, G. Peng, C. Gervais, Y. Ein-Eli and M. Shalom, Layered Boron–Nitrogen–Carbon–Oxygen Materials with Tunable Composition as Lithium-Ion Battery Anodes, *ChemSusChem*, 2018, **11**, 2912–2920, DOI: **10.1002/CSSC.201801438**.

43 D. A. Evans, A. G. McGlynn, B. M. Towlson, M. Gunn, D. Jones, T. E. Jenkins, R. Winter and N. R. J. Poolton, Determination of the optical band-gap energy of cubic and hexagonal boron nitride using luminescence excitation spectroscopy, *J. Phys.:Condens. Matter*, 2008, **20**, 075233, DOI: **10.1088/0953-8984/20/7/075233**.

44 X. Blase, A. Rubio, S. G. Louie and M. L. Cohen, Stability and Band Gap Constancy of Boron Nitride Nanotubes, *Europhys. Lett.*, 1994, **28**, 335, DOI: **10.1209/0295-5075/28/5/007**.

45 A. Zunger, A. Katzir and A. Halperin, Optical properties of hexagonal boron nitride, *Phys. Rev. B:Condens. Matter Mater. Phys.*, 1976, **13**, 5560, DOI: **10.1103/PhysRevB.13.5560**.

46 L. Song, L. Ci, H. Lu, P. B. Sorokin, C. Jin, J. Ni, A. G. Kvashnin, D. G. Kvashnin, J. Lou, B. I. Yakobson and P. M. Ajayan, Large-scale growth and characterization of atomic hexagonal boron nitride layers, *Nano Lett.*, 2010, **10**, 3209–3215, DOI: **10.1021/NL1022139**.

47 S. Kumar, S. Rajawat, P. Ojha, R. Purohit and M. M. Malik, Study of the effect of urea concentration on optical properties of Boron Carbon Oxynitride (BCNO) nanophosphor, *Optik (Stuttgart, Ger.)*, 2021, **232**, 166522, DOI: **10.1016/J.IJLEO.2021.166522**.

48 X. Zhang, Z. Lu, J. Lin, Y. Fan, L. Li, X. Xu, L. Hu, F. Meng, J. Zhao and C. Tang, Spectra Properties of BCNO Phosphor Prepared by a Two-Step Method at Low Sintering Temperature, *ECS J. Solid State Sci. Technol.*, 2013, **2**, R39–R43, DOI: **10.1149/2.012303JSS**.

49 B. W. Nuryadin, I. D. Faryuni, F. Iskandar and M. Abdullah, Khairurrijal, Effect of Silica Nanoparticles on the Photoluminescence Properties of BCNO Phosphor, *AIP Conf. Proc.*, 2011, **1415**, 171–174, DOI: **10.1063/1.3667249**.

50 K. M. M. O. Watanabe, S. Itoh and T. Sasaki, Visible-Light-Emitting Layered BC2N Semiconductor, *Phys. Rev. Lett.*, 1996, **77**, 2846, DOI: **10.1103/PHYSREVLETT.77.2846**.

51 H. Chen, Z. Zhao, J. Ding, X. Ding, Y. Cao and Y. Wang, Synthesis and spectral properties of rare-earth free tunable full-color-emitting Si-BCNO phosphors, *J. Lumin.*, 2018, **201**, 90–97, DOI: **10.1016/J.JLUMIN.2018.04.029**.

52 T. Ogi, Y. Kaihatsu, F. Iskandar, W. N. Wang and K. Okuyama, Facile synthesis of new full-color-emitting BCNO phosphors with high quantum efficiency, *Adv. Mater.*, 2008, **20**, 3235–3238, DOI: **10.1002/adma.200702551**.

53 X. Liu, S. Ye, Y. Qiao, G. Dong, Q. Zhang and J. Qiu, Facile synthetic strategy for efficient and multi-color fluorescent BCNO nanocrystals, *Chem. Commun.*, 2009, 4073–4075, DOI: **10.1039/B904567H**.

54 W. Lei, D. Portehault, R. Dimova and M. Antonietti, Boron carbon nitride nanostructures from salt melts: Tunable

water-soluble phosphors, *J. Am. Chem. Soc.*, 2011, **133**, 7121–7127, DOI: **10.1021/JA200838C**.

55 N. Tripathi, M. Yamashita and T. Akai, Synthesis and improved emission characteristics of BCNO@silica composites, *J. Mater. Chem. C*, 2013, **2**, 622–625, DOI: **10.1039/C3TC31964D**.

56 C. Ren, X. Zhang, L. Zhou, Z. Lu, J. Lin, X. Xu, L. Li, X. Zhang, Y. Xue, F. Meng, J. Zhao and C. Tang, Preparation optimization and spectral properties of BCNO phosphors with high quantum efficiency, *J. Lumin.*, 2014, **153**, 338–342, DOI: **10.1016/J.JLUMIN.2014.03.044**.

57 M. Rakshita, A. A. Sharma, P. P. Pradhan, K. A. K. Durga Prasad, K. Jayanthi and D. Haranath, Highly efficient and self-activating Zn3V2O8 phosphor for the fabrication of cool-white light emitting devices, *Ceram. Int.*, 2023, **49**, 16775–16785, DOI: **10.1016/j.ceramint.2023.02.038**.

58 P. P. Pradhan, R. Muddamalla, A. A. Sharma, D. P. Durga, U. K. Khanapuram, R. K. Rajaboina and H. Divi, Rare-Earth Ion-Activated Nanostructured Fluorescent Marker for Easy Naked Eye Detection and Swift Imaging of Latent Fingerprints, *ACS Appl. Nano Mater.*, 2023, **6**, 19767–19776, DOI: **10.1021/acsanm.3c03578**.

59 W. Pan, G. Ning, X. Zhang, J. Wang, Y. Lin and J. Ye, Enhanced luminescent properties of long-persistent Sr2MgSi2O7:Eu2+, Dy3+ phosphor prepared by the co-precipitation method, *J. Lumin.*, 2008, **128**, 1975–1979, DOI: **10.1016/J.JLUMIN.2008.06.009**.

60 P. Dorenbos, Mechanism of persistent luminescence in Sr2MgSi2O7:Eu2+; Dy3+, *Phys. Status Solidi A*, 2005, **242**, R7–R9, DOI: **10.1002/PSSB.200409080**.

61 J. Hölsä, M. Kirm, T. Laamanen, M. Lastusaari, J. Niittykoski and P. Novák, Electronic structure of the Sr2MgSi2O7:Eu2+ persistent luminescence material, *J. Lumin.*, 2009, **129**, 1560–1563, DOI: **10.1016/J.JLUMIN.2009.04.042**.

62 K. Van Den Eeckhout, A. J. J. Bos, D. Poelman and P. F. Smet, Revealing trap depth distributions in persistent phosphors, *Phys. Rev. B:Condens. Matter Mater. Phys.*, 2013, **87**, 045126, DOI: **10.1103/PHYSREVB.87.045126**.

63 A. J. J. Bos, Thermoluminescence as a Research Tool to Investigate Luminescence Mechanisms, *Materials*, 2017, **10**, 1357, DOI: **10.3390/MA10121357**.

64 J. Xue, T. Hu, F. Li, F. Liu, H. M. Noh, B. R. Lee, B. C. Choi, S. H. Park, J. H. Jeong and P. Du, Suppressed Self-Reduction of Manganese in Mg2SnO4 *via* Li+ Incorporation with Polychromatic Luminescence for Versatile Applications, *Laser Photon. Rev.*, 2023, **17**, 2200832, DOI: **10.1002/LPOR.202200832**.

65 E. Y. Andrei, A. Katzir and J. T. Suss, Point defects in hexagonal boron nitride. III. EPR in electron-irradiated BN, *Phys. Rev. B:Condens. Matter Mater. Phys.*, 1976, **13**, 2831, DOI: **10.1103/PhysRevB.13.2831**.

66 K. Atobe, M. Honda, M. Ide, H. Yamaji, T. Matsukawa, N. Fukuoka, M. Okada and M. Nakagawa, Point defects in cubic boron nitride after neutron irradiation, *Jpn. J. Appl. Phys.*, 1993, **32**, 2102–2104, DOI: **10.1143/JJAP.32.2102**.

67 M. Hubáček, T. Sato and T. Ishii, A Coexistence of Boron Nitride and Boric Oxide, *J. Solid State Chem.*, 1994, **109**, 384–390, DOI: **10.1006/JSSC.1994.1117**.